A compact and compliant electrorheological actuator for generating a wide range of haptic sensations

IOP Publishing
Smart Materials and Structures
Smart Mater. Struct. 29 (2020) 055028 (16pp)
https://doi.org/10.1088/1361-665X/ab710c

A compact and compliant electrorheological actuator for generating a wide range of haptic sensations

Alex Mazursky[1], **Jeong-Hoi Koo**[1,3] and **Tae-Heon Yang**[2]

[1] Department of Mechanical and Manufacturing Engineering, Miami University, Oxford, OH 45056, United States of America
[2] Department of Electronic Engineering, Korea National University of Transportation, Chungju-si, Chungbuk, 27469, Republic of Korea

E-mail: koo@miamioh.edu

Received 20 July 2019, revised 16 December 2019
Accepted for publication 28 January 2020
Published 6 April 2020

Abstract

Robust haptic devices that can convey the entire spectrum of human touch perception are necessary to afford realistic haptic experiences. For vivid and immersive interaction, a combination of both tactile and kinesthetic information must be presented to users. While vibrotactile feedback has become ubiquitous in today's handheld devices, traditional kinesthetic actuators present significant challenges to miniaturization. Moreover, only limited success has been achieved in developing haptic actuators capable of conveying both tactile and kinesthetic sensations for small consumer electronics. Therefore, this study presents a compact actuator based on electrorheological (ER) fluid for generating a wide range of concurrent kinesthetic and tactile feedback. The design focus for the proposed actuator is to activate multiple operating modes of ER fluid to maximize the force generated by the actuator within a given small size constraint. To this end, the design incorporated two ground electrodes (a stationary ring electrode and a movable electrode attached to a spring element) for tuning the fluid's yield stress in both flow and squeeze modes. After fabricating a prototype actuator, testing was performed with a dynamic mechanical analyzer (DMA) and an accelerometer to evaluate its ability to produce a wide range of kinesthetic feedback, as well as distinct vibrotactile feedback up to the limit of human perception. The results of kinesthetic testing indicate that the actuator can generate large forces (6.2 N maximum at 4 kV) at rates greater than the just-noticeable difference, indicating that the actuator can convey a wide range of kinesthetic sensations. Tactile evaluation using DMA and the processed acceleration response demonstrated that the actuator can generate both low and high frequency (up to 300 Hz) vibrotactile sensations at perceivably high intensity.

Keywords: haptic actuator, electrorheological fluid, kinesthetic feedback, tactile feedback, multimodal feedback

(Some figures may appear in colour only in the online journal)

1. Introduction

In the field of human–computer interaction, haptic devices are becoming increasingly important for their ability to transmit meaningful information through touch sensation between operators and environments. When paired with visual and audio feedback, the haptics of being able to feel and manipulate objects in an environment offers users a rich, immersive experience [1]. Thus, the benefits of haptic feedback have been realized in a wide range of applications, including teleoperation, simulators, gaming and entertainment [2–5].

[3] Author to whom any correspondence should be addressed.

In commercial touchscreen devices, haptic technology is used to provide touch feedback through vibrations, or vibrotactile feedback. While vibrotactile feedback can provide primitive sensations, vibration alone is insufficient for conveying comprehensive haptic feedback. For haptic feedback to be completely immersive, a combination of two feedbacks is necessary: (1) tactile and (2) kinesthetic [6]. Tactile feedback is sensed by mechanoreceptors in the skin and provides information pertaining to surface roughness and textures. Kinesthetic feedback is perceived as forces and torques by muscles, tendons, and joints and affords information about position and movement. Thus, when designing interfaces based on touch, both modes of haptic feedback (multimodal) should be present to convey realistic haptic sensations by taking full advantage of human sensing capability.

Despite much research on the development of new haptic devices in recent years, most studies present methods for conveying kinesthetic or tactile sensations independently [7, 8]. Furthermore, while tactile actuators have been extensively implemented into consumer devices, the development of kinesthetic actuators has been comparatively slow. Many of the kinesthetic devices proposed in current research are based upon alternating current/direct current (AC/DC) motors [9–11]. However, kinesthetic motors are restricted to immobile applications due to their size and power requirements. Moreover, using high-torque motors for feedback requires additional attention toward control stability and operator safety [12, 13].

Many researchers have concluded that to avoid the shortcomings of traditional actuation, advanced materials and new methods must be engineered to make valuable devices with simultaneous kinesthetic and tactile feedback [14, 15]. For example, smart materials and their adaptable properties offer a mechanically simpler solution. Piezoelectric beams have become popular for generating tactile feedback, but provide insufficient forces for kinesthetic feedback [16, 17]. Contrarily, shape memory alloys can provide variable kinesthetic feedbacks in bending and pulling, but do not respond quickly enough to trigger tactile sensations [18, 19]. Between these two smart materials, a gap emerges; to attain concurrent tactile and kinesthetic sensations, the ideal material must be capable of generating large forces at fast rates. To this end, smart fluids pose an attractive candidate for their rapid and stable response and ability to generate high yield stresses through their tunable viscosity.

Magnetorheological (MR) fluid has been the basis for numerous haptic devices [20–23]. Most of these MR-based devices were designed as feasibility studies and would be challenging to scale down for personal electronics due to the size required of the solenoid coils. Yang *et al* [24] investigated the feasibility of miniaturizing an MR fluid-based device for combined kinesthetic and tactile feedback. In following parametric studies, this button-type device was reduced into a module that is small enough for mobile devices while maintaining the resolution and range of haptic feedback [25, 26]. Despite optimization, designing MR actuators still requires precise manufacturing to produce the miniature coil. Ultimately, the size of the solenoid has been the biggest roadblock for miniaturizing MR devices.

Analogous to MR fluid, electrorheological (ER) fluid's viscosity is dependent upon the magnitude of applied electric field. Through this principle, ER fluid may be demonstrated to be better suited for small-scale applications. While ER fluid offers fast response times, low power consumption and stability on the order of MR fluid, ER fluid relies on simpler electrical control; only two electrodes spaced on the order of 1 mm apart are required, lending itself to smaller, more mobile designs [27–29]. Past works have investigated ER fluid for its ability to convey haptic feedback [30–33]. However, previous studies have not focused on device miniaturization or providing combined tactile and kinesthetic feedback. To demonstrate feasibility, Mazursky *et al* [34] experimentally tested a small button-type actuator based on ER fluid in flow mode. In a subsequent study, Mazursky *et al* [35] reduced the actuator's thickness to 5.4 mm and validated the actuator's ability to generate kinesthetic and tactile sensations through experimentation and analytical modeling. Though, for the haptic device developed in this study to be implemented as a robust kinesthetic actuator, it is desirable to widen the range of output forces as much as possible without greatly increasing the size or complexity of the design.

Beyond producing a wide range of force outputs for a variety of kinesthetic sensations, a comprehensive haptic device must be able to produce vibrations in a wide frequency range for delivering a variety of vibrotactile sensations. There are four mechanoreceptors in human skin responsible for detecting tactile sensations: Meissner corpuscle, Pacinian corpuscle, Merkel disk and Ruffini endings. Together, these receptors account for sensing low to high frequency vibrations (reliably up to 300 Hz), as well as static pressures [36]. By utilizing frequencies across the range of human perception, meaningful and familiar sensations can be communicated to users and greatly enhance device immersion [37, 38]. Traditional tactile actuators, such as linear resonant actuators, are designed to operate within a narrow resonant range and therefore cannot stimulate across the entire human tactile spectrum. Thus, the dynamic and tunable behavior of ER fluid may afford a wider vibration range and vivid sensations.

To overcome the outlined limitations of conventional haptic actuators, this study presents the design of an ER actuator capable of producing a sufficiently wide range of forces for kinesthetic feedback and variable vibrotactile feedback up to 300 Hz. Moreover, the device's form is compact (6 mm thickness), lending itself to mobile applications. To increase the force production, this study introduces a design modification to the 'flow-mode' device that yields a region of squeeze mode operation in addition to flow mode, thus enabling a multiple or mixed-mode activation of ER fluids. A prototype was designed, fabricated and tested using a dynamic mechanical analyzer (DMA) fitted with an accelerometer with a goal of characterizing the device's ability to convey kinesthetic and vibrotactile feedbacks produced by varying the applied voltage magnitude and frequency. In the following section, the design and fabrication of the mixed-mode prototype actuator is described. Next, a mathematical model of the actuator's performance is derived and used to simulate the actuator's behavior. The experiments to measure the actuator's force along its stroke as well as high frequency vibration is then presented, followed by a discussion of the results.

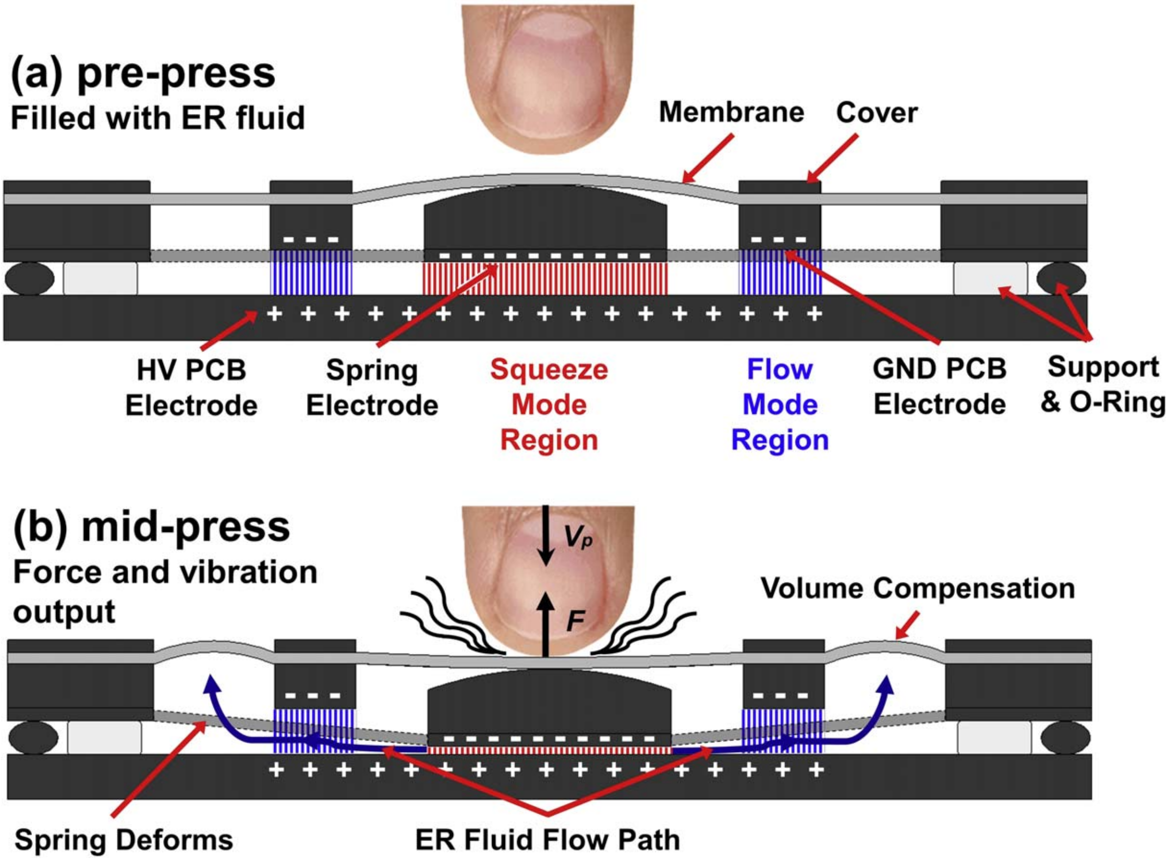

Figure 1. Cross-section view of the working principle of the cylindrical haptic actuator operating in mixed modes (a) pre-press and (b) mid-press.

2. Design and fabrication

The design of the haptic actuator is motivated by maintaining a thin form for embedding in mobile applications, while increasing the range of force outputs from the previous design iteration (described in [35]). To do so, a region of squeeze mode is introduced. This section first details the working principles behind using ER fluid in mixed flow and squeeze modes to produce haptic feedback. It then proposes the structural design of the actuator. Finally, this section presents the fabricated prototype.

2.1. Working principles

The design focus of the current study is to greatly increase the haptic actuator's range of force outputs while constraining the device's thickness. In comparison with the previous design, this study implements a region of ER fluid in squeeze mode, in addition to the preceding flow mode, to produce large forces in a small gap. It is well established that squeeze mode is the most effective method of yielding high actuation forces across a small displacement [39]. Introducing squeeze mode to the actuator's design may therefore increase the range of forces produced by the actuator.

Figure 1 illustrates the cross-section and working principle of the proposed, cylindrical mixed-mode haptic actuator. The mixed-mode design features the same flow mode principle as in the previous design, which can be found in [35]. However, in contrast with previous design, the newly proposed, mixed-mode actuator contains an additional grounded 'spring' electrode below the contact surface and a larger, disk-shaped charged electrode surface in order to activate an additional operating mode of ER fluid (i.e. squeeze mode, shown in red in figure 1), and therefore produce a wider range of force outputs. When a user presses upon the membrane contact surface, the grounded spring electrode is displaced vertically, squeezing the fluid between the spring electrode and high voltage (HV) electrode. Due to the pressure gradient during interaction, fluid flows radially outward through parallel fixed electrodes (i.e. flow mode, shown in blue in figure 1). Hence, the actuator operates in both squeeze and flow modes. To account for the volume change due to indentation, the device features radial slots allowing the membrane between the slots to deform elastically, forming a reservoir (see figure 1(b)). Upon relieving pressure at the contact surface, the reservoir depresses, and the actuator returns to its pre-pressed state through the elastic nature of the electrode spring and membrane. When voltage is supplied to the electrodes, the ER fluid in the squeeze and flow mode regions form fibrous networks parallel to the field lines. This microstructural transformation results in a yield stress with magnitude corresponding to the applied field strength. Therefore, the force experienced by the user's finger during interaction is a direct consequence of the applied voltage. As

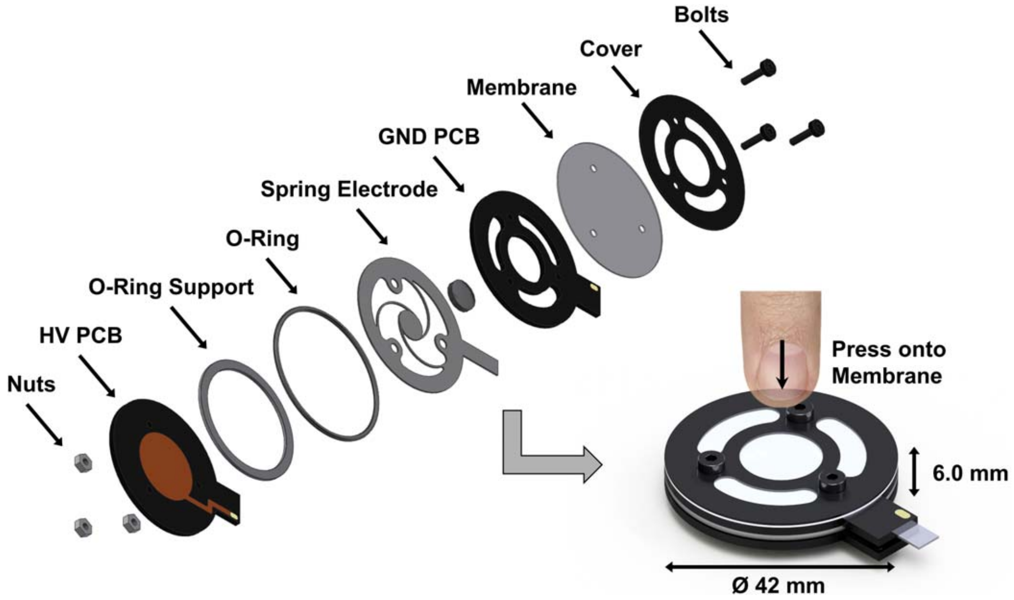

Figure 2. Exploded view drawing of the mixed-mode haptic actuator.

the magnitude of the voltage increases, the force required to cause the fluid to flow increases, indicating a range of kinesthetic feedbacks. By introducing a frequency to the applied voltage, the resistive force may oscillate, resulting in various tactile feedbacks. Thus, the user may feel a dynamic range of simultaneous kinesthetic and tactile sensations.

2.2. Structural design

Figure 2 shows an exploded view drawing of the proposed haptic actuator's components and assembly. As shown, the main structure of the device is composed of printed circuit boards (PCBs). By integrating the device's structure with the electrical components, the design remains mechanically simple and compact. The device's internal volume is filled with giant ER (GER) fluid. The bottom PCB has a large disk-shaped electrode and is rated for HVs. A plastic ring fits between the HV PCB and the spring electrode, acting as a spacer for maintaining the electrode gap distance and providing structure to an O-ring seal. A spring steel electrode (SUS 304) that can deform elastically for small displacements is used to introduce a region of squeeze mode. To prevent binding between the spring electrode and HV PCB due to electrostatic forces, a small (1 mm diameter, 0.35 mm thick) silicone film is adhered to the spring electrode. A small plastic knob is attached to the top of the spring electrode and contact membrane to couple their displacements, as well as pre-strain the membrane to reduce its nonlinearity. The top PCB has an annulus-type electrode and shares a common ground with the spring electrode (GND PCB). A flexible silicone membrane (PDMS) is bonded to the top of the GND PCB by a thin film of acrylic tape (3M^{TM} VHB 4910). Nylon nuts and bolts fasten the device and compress the O-ring and membrane to seal the ER fluid inside. Thus, the membrane doubles as a seal and the device's contact surface. Tabs on the PCBs and spring electrode allow for HV and GND leads to supply the device with electrical inputs. The assembled device has a diameter of 42 mm and a thickness of 6.0 mm.

2.3. Fabrication of prototype

Figure 3 presents the device's fabricated individual components and assembled prototype actuator. The device functions as a button-type actuator and is composed of two electrode PCBs, a plastic spacer and O-ring, a thin-film silicone and acrylic tape membrane, and a plastic cover. The HV electrode radius measures 11 mm.

Additionally, a compliant spring electrode is placed inside the device. Figure 4 shows the fabricated spring electrode. As shown, three thin beams arranged in a spiral pattern allow for small displacements (into the page) at the electrode's center. The radius of the spring electrode measures 4.7 mm. The thickness of the spring electrode was determined through prototyping and experimentation. A 0.2 mm and a 0.3 mm thick electrode adhered together was determined to offer sufficient returning force without overpowering the resistive force produced by the ER effect.

The maximum indentation depth of the actuator is 1 mm. The device was designed and manufactured with a goal of minimizing thickness to convey a wide range of kinesthetic and tactile sensations in a compact form. Introducing a squeeze mode to the actuator comes at little sacrifice to device thickness while adding functionality through a wider range of meaningful sensations.

3. Mathematical modeling and simulation

To understand the mixed-mode actuator's behavior from a generalizable standpoint, a mathematical model was developed based on the device's fundamental behavior. Three factors contribute to the forces presented by the actuator:

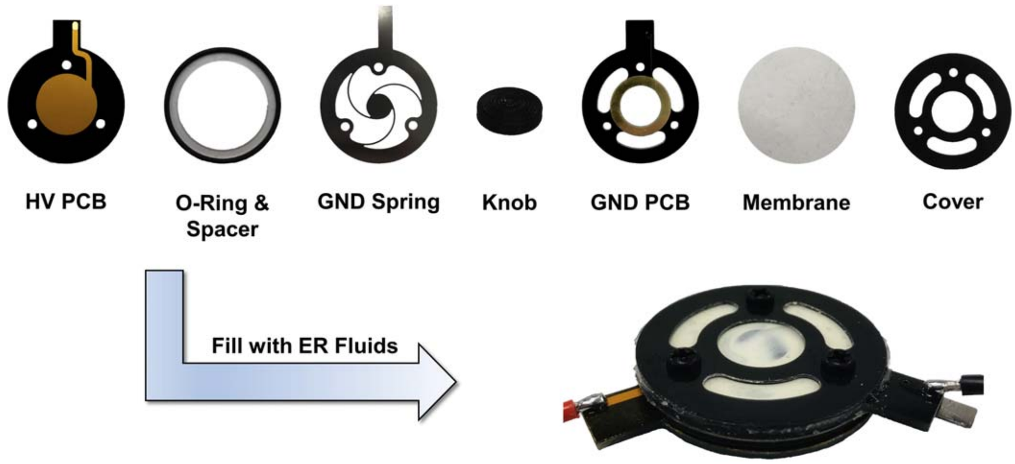

Figure 3. Fabricated components and mixed mode actuator assembly.

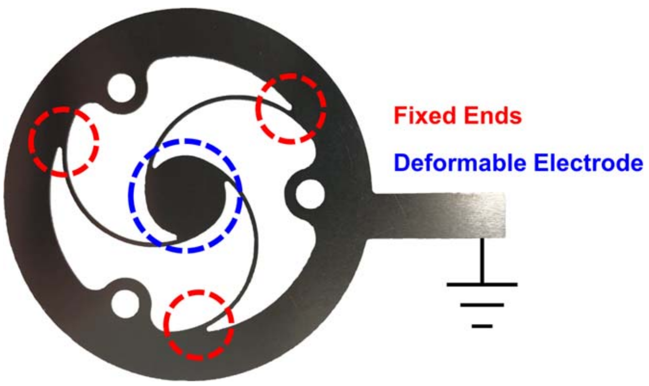

Figure 4. Fabricated elastic spring electrode.

(1) the yielding behavior of ER fluid in mixed-modes, and the deformation of the (2) electrode spring and (3) membrane due to volume compensation. Thus, the first subsection presents the literature's established flow and squeeze mode models for relating input voltage to output force. The following subsection presents a numerical approach to determining the spring electrode's stiffness coefficient in the vertical direction. Then, the force due to the membrane's deformation is derived. Finally, a comprehensive model of the actuator's force output is implemented into a numerical framework and used to simulate the actuator's behavior.

Figure 5 presents an axisymmetric schematic of the actuator's mechanics. As shown, there are two distinct regions defined by electrode configuration: a region of squeeze mode (red annotations) where the grounded spring electrode moves relative to the fixed HV electrode and a region of flow mode (blue annotations) where both the grounded and charged electrodes remain stationary. When the user presses upon the actuator, fluid flows between the electrodes when the pressure gradient exceeds the fluid's yield stress. Thus, the total force due to fluid flow may be expressed by the sum of the forces associated with each mode and is felt at the user's fingertip. In addition to the fluid forces, the electrode spring and elastic membrane contribute to the actuator's total resistive force.

A comprehensive model for the force felt by the user is developed by analyzing the individual forces, and may be described as

$$F_{\text{total}} = F_{\text{squeeze}} + F_{\text{flow}} + c_{\text{squeeze}}\dot{z} + c_{\text{flow}}\dot{z} + k_z z + F_{\text{membrane}}, \tag{1}$$

where F_{squeeze} and F_{flow} are the controllable, field-dependent forces associated with each yielding in each mode, z denotes vertical displacement, $c_{\text{squeeze}}\dot{z}$ and $c_{\text{flow}}\dot{z}$ are the viscous damping forces, $k_z z$ is the vertical spring force of the elastic spring electrode, and F_{membrane} is the force due to the membrane's deformation due to volume compensation. The following subsections describe the mechanics behind these forces in depth.

3.1. Analytical model of ER fluid in mixed-mode

Over the years, many models have been proposed to describe ER fluid's behavior [40–45]. Of these models, the earliest conceived and most prevalent in application has been the Bingham plastic model [41]. In the Bingham plastic model, the fluid's base viscosity is taken to be constant. For the fluid to flow, the field-dependent yield stress must be overcome. Upon stressing ER fluid past its yield point, it begins to flow like a Newtonian fluid with a constant viscosity. The Bingham plastic model is a steady state model that takes the fluid to be in the post-yield state and flowing at a constant shear rate [40, 41, 46]. Thus, the Bingham model does not account for pre-yield behavior or the shear thickening/thinning effects observed at high shear rates, on which succeeding models have focused [42–45]. However, for the device proposed in this study which operates in post-yield and a relatively low, constant shear rate, the Bingham plastic model is sufficient at capturing the actuator's behavior. Hence, this study applies squeeze and flow mode models based upon the Bingham plastic model.

The total force produced in the squeeze mode region is represented as [47, 48]

$$F_{\text{total\_squeeze}}(t) = F_{\text{squeeze}}(t) + c_{\text{squeeze}}(t)\dot{z}(t), \tag{2}$$

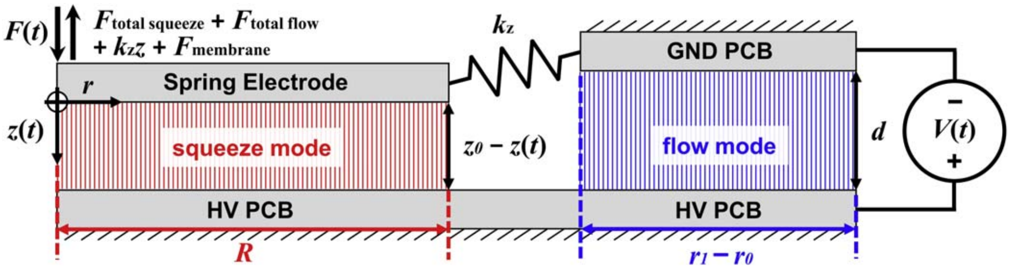

Figure 5. Axisymmetric view of the mixed-mode mechanism and geometric parameters.

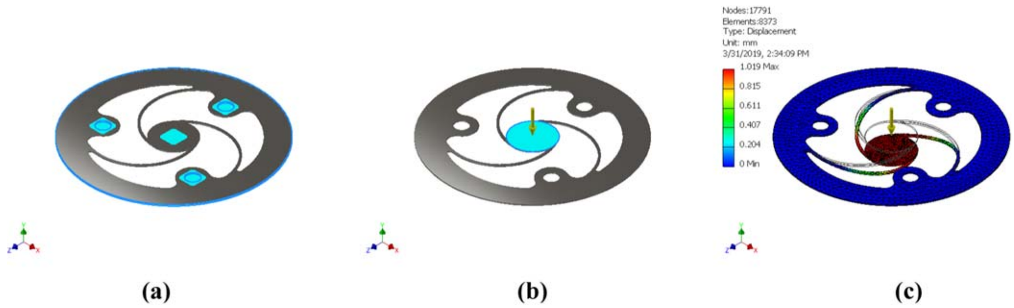

Figure 6. Steps in the finite element analysis process for characterizing the electrode spring: (a) fixed constraints set at the perimeter and through-holes, (b) loading assigned at the electrode's center, and (c) solving for the displacement result in the y-direction.

where

$$F_{\text{squeeze}}(t) = \frac{4}{3}\frac{\pi R^3}{z_0 - z(t)}\tau_y(E)\,\text{sgn}(\dot{z}(t))$$
$$c_{\text{squeeze}}(t) = \frac{3}{2}\frac{\pi\mu R^4}{(z_0 - z(t))^3}. \qquad (3)$$

In this formulation, $c_{\text{squeeze}}(t)$ is the damping coefficient of ER fluid due to viscous flow in the off-state, μ is the fluid's dynamic viscosity, $z(t)$ is the current displacement of the user's finger, z_0 is the initial squeeze electrode gap, and R is the radius of the spring electrode (and the radius of the piston that drives the flow). $F_{\text{squeeze}}(t)$ is the force associated with the fluid's active response and $\tau_y(E)$ is the fluid's yield stress and depends upon the applied voltage $V(t)$.

Similarly, the total force generated in the flow region is approximated by a parallel plate approximation by taking the annular electrodes to behave as a rectangular duct. While previous work applies the parallel plate approximation to a cylindrical configuration [49], this study applies the approximation to a disk configuration to mitigate nonlinearities associated with radial flow. By taking the average radius to be the duct width, an approximation of equivalent rectangular duct flow may be made due to the small relative difference between the inner and outer radii, r_0 and r_1. Thus the total force produced in the flow region is represented as

$$F_{\text{total\_flow}}(t) = F_{\text{flow}}(t) + c_{\text{flow}}(t)\dot{z}(t), \qquad (4)$$

where

$$F_{\text{flow}}(t) = 2\frac{\pi R^2 L}{d}\tau_y(E)\,\text{sgn}(\dot{z})$$
$$c_{\text{flow}}(t) = \frac{12\mu\pi^2 R^4 L}{bd^3}. \qquad (5)$$

In the above, L is the electrode length for an equivalent rectangular duct, or the difference between the outer radius r_1 and inner radius r_0, b is the equivalent electrode width, or the average circumference of the annular electrode, and d is the fixed electrode gap.

3.2. Numerical model of electrode spring constant

A finite element method (FEM) model was developed to determine the force produced by the electrode spring with respect to its displacement. Figure 6 shows the modeling process. First, the geometry was drawn in Autodesk Inventor™ software. The fixed ends and compressed section of the electrode spring were prescribed fixed boundary conditions. An applied force was assigned perpendicular to the center of the spring electrode.

Table 1 provides mechanical properties of SUS 304. These material parameters were assigned to the modeled electrode to match the fabricated electrode.

To determine the force–displacement relation for the spring electrode, a range of applied forces were prescribed, and the resultant displacement was found. This was performed for spring electrode thicknesses of both 0.2 and 0.3 mm and the data points were fit with linear curves, as shown in figure 7. To estimate the force produced by the fabricated electrode spring (0.2 and 0.3 mm thick electrodes adhered together), the individual 0.2 and 0.3 mm thick curves are added together. Therefore, the spring constant k_z is determined by the slope of the total response. For the total spring, the spring constant is predicted to be $1160\,\text{N m}^{-1}$.

3.3. Analytical modeling of membrane mechanics

Having determined force–displacement models for the ER fluid and electrode spring, this subsection presents an

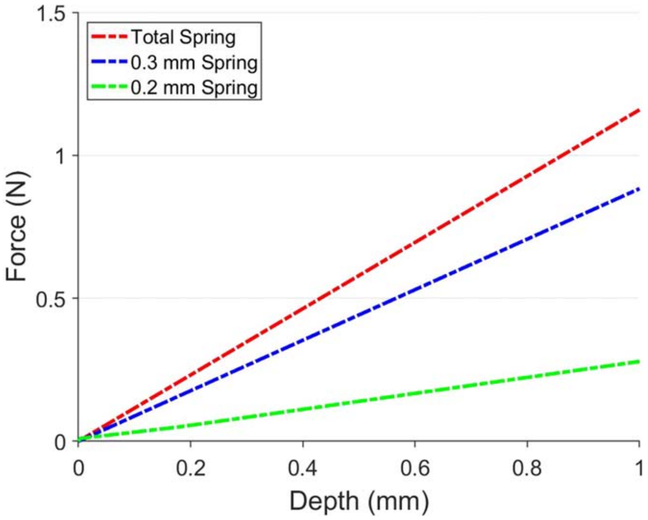

Figure 7. Force produced by displacing the spring electrode generated by FEM.

Table 1. Mechanical properties of Type 304 stainless steel (SUS 304) used in the FEM simulation.

Parameter	Value
Behavior	Isentropic
Young's modulus	193 GPa
Poisson's ratio	0.29
Density	8000 kg m^{-3}

analytical model of the elastic forces due to membrane's deformation due to volume compensation. As described in section 2.2, the membrane is comprised of two layers: contact and adhesive. The silicone contact layer is taken to behave as a nonlinear film without pre-strain, whereas the adhesive acrylic tape layer is taken to behave linearly due to pre-strain. The total analytical result is found by superposing the force-displacement curves produced by each layer.

The volume compensation membrane's radial slot geometry is approximated as three rectangular films with high aspect ratios. The load-deflection relation for the nonlinear PDMS layer without pre-strain is represented as [50]

$$q = \frac{4Eh}{3x^4(1-\nu^2)}w^3, \tag{6}$$

where q is the pressure exerted on the membrane surface, E is the elastic modulus, h is the membrane thickness, x is the membrane width, ν is Poisson's ratio, and w is the deflection at the membrane's midpoint. The compensating membrane's deflection is related to the indentation depth by conservation of volume. Similarly, the load deflection for a pre-stressed rectangular membrane is given as [50]

$$q = 2\frac{\sigma_0 h}{x^2}w + \frac{4Eh}{3x^4(1-\nu^2)}w^3, \tag{7}$$

where σ_0 is the pre-stress.

Table 2. Parameters of the membrane model.

Parameter	Symbol	Value (PDMS)	Value (VHB)
Width	x	2.3 mm	2.3 mm
Thickness	h	0.43 mm	0.08 mm
Pre-stress	σ_0	0 kPa	180 kPa
Elastic modulus	E	250 kPa	60 kPa
Poisson's ratio	ν	0.50	0.49

Table 3. Parameters of the mixed-mode haptic actuator.

Parameter	Symbol	Value
Static electrode gap	d	1.8 mm
Inner electrode radius	r_0	7.5 mm
Outer electrode radius	r_1	11 mm
Initial electrode gap	z_0	1.3 mm
Spring electrode radius	R	4.7 mm
Viscosity of GER fluid	μ	0.060 Pa s
Velocity of indentation	V_p	1 mm s^{-1}
Final indentation depth	δ_f	1 mm

The total force posed by the membrane is found by relating pressure to force by the area of the volume compensation region. Table 2 shows parameters for computing the force produced by membrane mechanics. The forces predicted by the membrane model were first validated by comparing to experiments performed without fluid inside the actuator (see [35] for in-depth analysis).

3.4. Numerical simulation of actuator performance

To simulate the actuator's performance, a MATLAB® script was written based on the modeling illustrated in the previous subsections. The model calculates the forces generated by the actuator over the duration of a 1 mm indentation, as described by equation (1). A GER scaling function was used to couple the applied electric field and the GER fluid's yield stress using properties provided by the manufacturer (Smart Materials Laboratory Ltd), such as a maximum yield stress of 80 kPa at 5 kV mm^{-1} [51]. The yield stress due to the applied field is used as an input to determine the force due to the ER effect. The parameters for simulating the ER effect are given in table 3. The values used are representative of the fabricated actuator and experimental test setup.

The computational model is supplied with voltage and frequency inputs and produces plots of the force generated by the actuator along its stroke. Figure 8(a) shows the force curves produced by the model when subjected to DC voltage inputs of 0, 1, 2, 3, and 4 kV. As shown, when no voltage is supplied to the simulated actuator, the greatest force produced is about 2.6 N at maximum indentation. When the maximum voltage is applied (4 kV DC), the output force at 1 mm depth increases to nearly 6.5 N. Figure 8(b) shows the predicted force profiles when the model is supplied with the same voltage range, pulsated at a sinusoidal frequency of 5 Hz. As shown, as the magnitude of the voltage increases, the

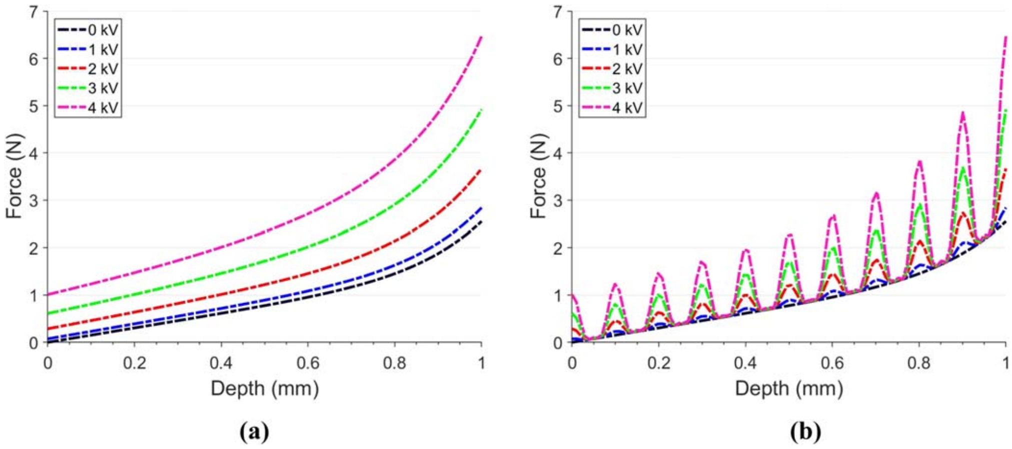

Figure 8. Results of the simulated actuator: force (N) versus depth (mm) along its stroke when subjected to (a) DC voltages and (b) 5 Hz sine functions.

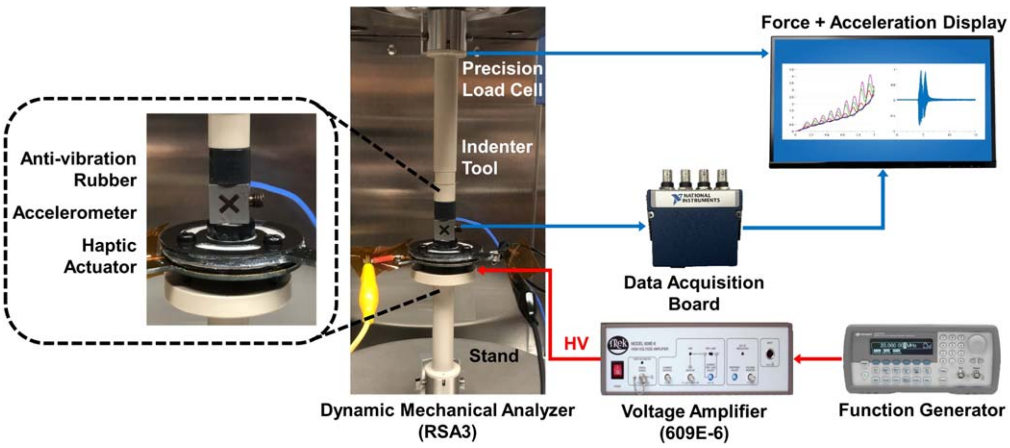

Figure 9. Experimental setup for evaluating the mixed mode device's kinesthetic and vibrotactile feedback.

amplitude of vibration increases as well. The vibrotactile profiles are bounded by the off-state and corresponding applied voltage curves shown in the kinesthetic result. The simulation results imply that the actuator can provide both kinesthetic and vibrotactile feedback.

4. Experimental evaluation

This section details the experimental methods used to evaluate the fabricated mixed-mode haptic actuator. The goal of these experimental studies is to characterize the device's ability to produce a wide range of kinesthetic and vibrotactile feedbacks. Experimental methods include compression testing with a DMA and vibration testing using an accelerometer. This section concludes by comparing the actuator's experimental and simulated performances.

4.1. Experimental setup

Compression testing was performed using a DMA (RSA3, TA Instruments) to evaluate the haptic actuator's performance. A function generator and voltage amplifier (Trek Model 609E-6, 1000 V/V) control the applied electric field, as shown in figure 9. This setup allowed for accurate force versus depth plots in a low frequency range (up to 10 Hz). As mentioned in the introduction section, the Pacinian corpuscles are sensitive to vibrations up to 300 Hz [36, 52]. However, the DMA is insufficient for measuring high frequency variations in force due to its rate of data collection. Thus, this study modified the experimental setup to measure the actuator's performance at higher frequencies within the limits of human perception (up to 300 Hz). To this end, an accelerometer (PCB Piezotronics 356A22) and a vibration isolating rubber were fitted between the DMA indenter and the contact surface of the device (see figure 9). With the addition of the accelerometer, the setup can accurately characterize the high frequency vibration response of the actuator. A data acquisition board (NI cDAQ9172) connected to a host computer is used to collect and process the data from the accelerometer. A 5 kHz sampling frequency was used, which is sufficiently greater than the frequencies rendered by the device to avoid aliasing. The performance was evaluated under different input voltage and frequency conditions using an indenter similar in size to a human finger. An indentation rate of 1 mm s^{-1} was used for all testing.

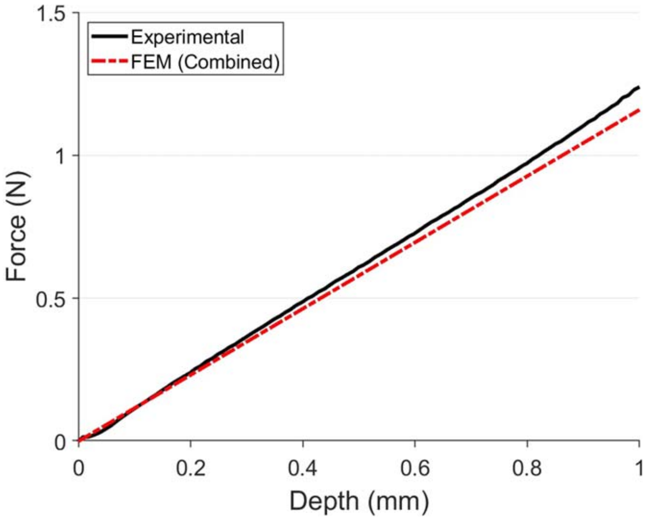

Figure 10. Comparison between the electrode spring's experimental response from dry testing and the FEM simulation response for the superposed 0.2 and 0.3 mm spring responses.

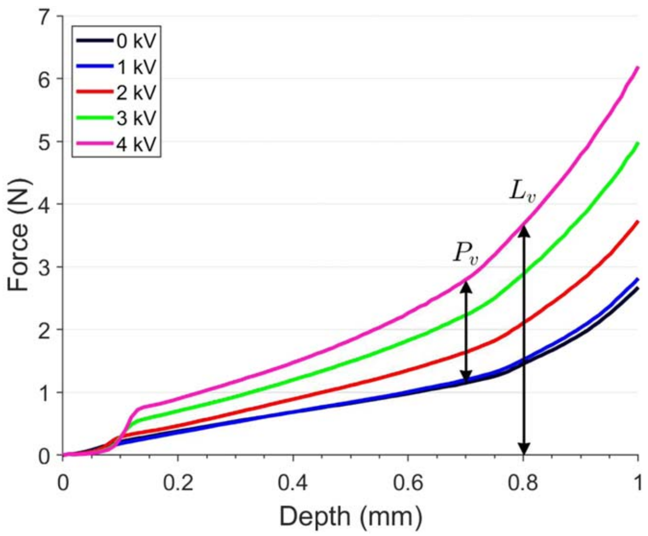

Figure 11. Experimental mixed mode kinesthetic results: force (N) versus depth (mm).

4.2. Electrode spring response

Dry testing was first performed with an actuator assembled without fluid inside the device to experimentally obtain the force-depth response of the electrode spring and contact membrane and compare the result with that of simulation. Figure 10 plots the FEM simulation and experimental electrode spring responses. The nearly linear experimental response indicates that the actuator's dry response is mostly dependent upon the electrode spring's linear elastic behavior. The FEM electrode spring model is demonstrated to be sufficiently accurate when plotted against the experimental response. The spring constant is experimentally found to be 1240 N m^{-1} (compared to the modeled constant of 1160 N m^{-1}).

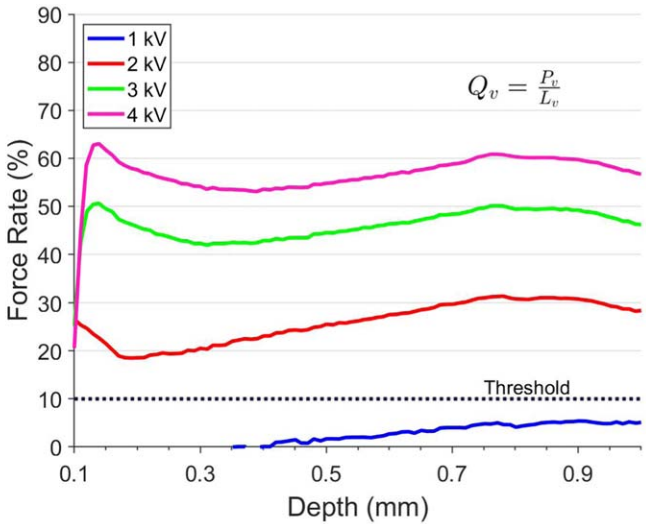

Figure 12. Measured mixed mode kinesthetic results: force rate (%) versus indentation depth (mm).

4.3. Evaluation of kinesthetic response

To test the device's ability to generate a wide range of stiffness, a kinesthetic testing protocol was developed and performed. First, the actuator's passive force was measured without applied voltage. The actuator was then subjected to high frequency (100 Hz) square waves to emulate a pulsating DC signal. The actuator's active response was measured for applied voltages between 0 V and peak amplitudes of 1, 2, 3 and 4 kV. These results are presented below in figure 11. As shown, the resistive force produced increases with the applied voltage and pressed depth. The passive resistive force was measured to be about 2.7 N at maximum depth. The maximum force produced was about 6.2 N under 4 kV load. Compared to higher voltages, the effect of applying 1 kV on the force profile is minimal.

Of additional note, within the first 0.1 mm of the stroke, the profiles follow a similar curve independent of applied voltage. This is due to a thin gap where fluid filled between the contact membrane and the spring electrode's spacer. To eliminate this lag, attention may be given during assembly to ensure a secure bond between the plastic spacer and acrylic tape. This prevents fluid from causing separation and ensures a coupled response. Thus, the ER effect is not realized until 0.1 mm into the stroke. However, it should be noted that this does not interfere with the quality of kinesthetic interaction. Prior psychophysical research suggests that the average differential threshold for the human finger to detect a difference in compliance (change in displacement per applied force) is 22% [53]. For a constant applied force and a 1 mm stroke, the minimum displacement change that a human may distinguish is about 0.22 mm. Thus, the transient 0.1 mm region at the start of the haptic actuator's stroke falls within this threshold. Therefore, the kinesthetic interaction is not diminished by this property of the device.

To further analyze the kinesthetic results from a haptic standpoint, the measured force rates are calculated as the metric for the just-noticeable difference (JND). The JND is a

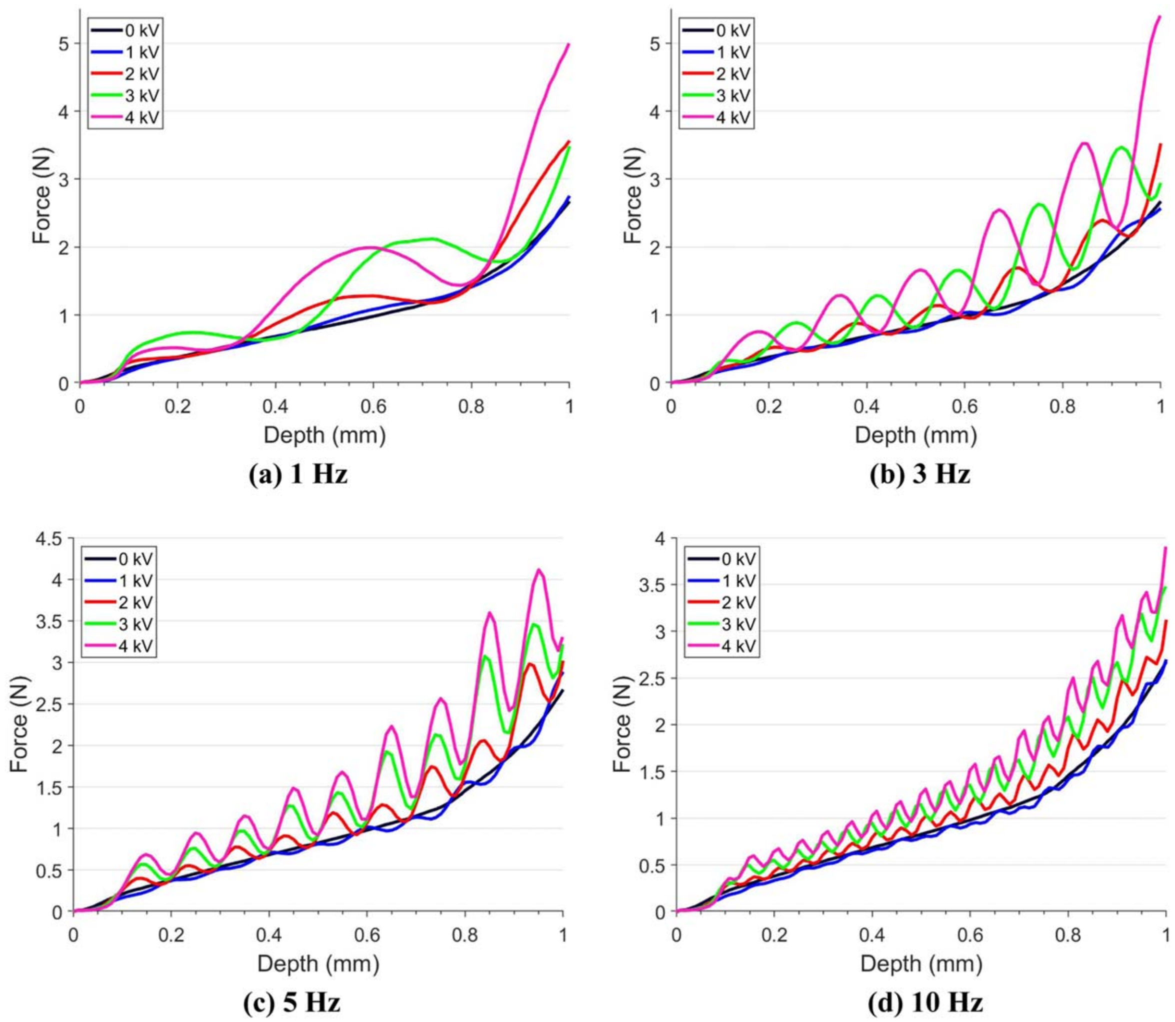

Figure 13. Experimental tactile results: force rate versus indentation depth (mm).

measure of the degree that the kinesthetic force must change for a difference to be perceived by a human. Force rate (Q_v) at a given depth is defined as the ratio of the difference between the maximum and minimum force (P_v) to the maximum force (L_v) at said depth

$$Q_v = \frac{P_v}{L_v}. \tag{8}$$

Figure 12 is produced by applying the force rate equation across all depths in the actuator's stroke. Beyond a depth of 0.1 mm, the force rates stabilize and follow a similar flat profile. The greatest force rate is produced by the 4 kV curve, which averages about 57%. The lowest force rate is generated by the 1 kV signal, which fell below the off-state curve for the first 0.35 mm of the stroke, resulting in a negative force rate. The threshold for which humans can consistently detect changes in force is about 7%–10% for forces between 0.5 and 200 N [54]. As indicated by the plot in figure 12, the proposed actuator can convey distinct and consistent kinesthetic feedback above the threshold for supplied voltages greater than 1 kV.

4.4. Evaluation of tactile response

To measure the actuator's vibrotactile response, sinusoidal voltage inputs were applied between 0 V and peak amplitudes of 1, 2, 3, and 4 kV. The vibrational response is evaluated using two techniques: (1) the force-depth data from the DMA is analyzed for low frequency responses and (2) the accelerometer data is processed for high frequency responses.

4.4.1. Low frequency. To measure the actuator's low frequency vibrotactile response, sinusoidal waveforms at frequencies of 1, 3, 5, and 10 Hz are supplied. Figure 13 presents the resultant force profiles for each set of frequencies and voltages. As seen in the figure, the force feedback responds harmonically when subjected to sinusoidal voltages. As the magnitude of the applied voltage increases, the amplitude of vibration increases as well. These results show that the actuator can convey controllable resistive forces over a range of low frequencies. Therefore, the actuator can communicate low-frequency vibrotactile feedback.

To further demonstrate the mixed-mode actuator's vibrotactile performance, its response may be compared to

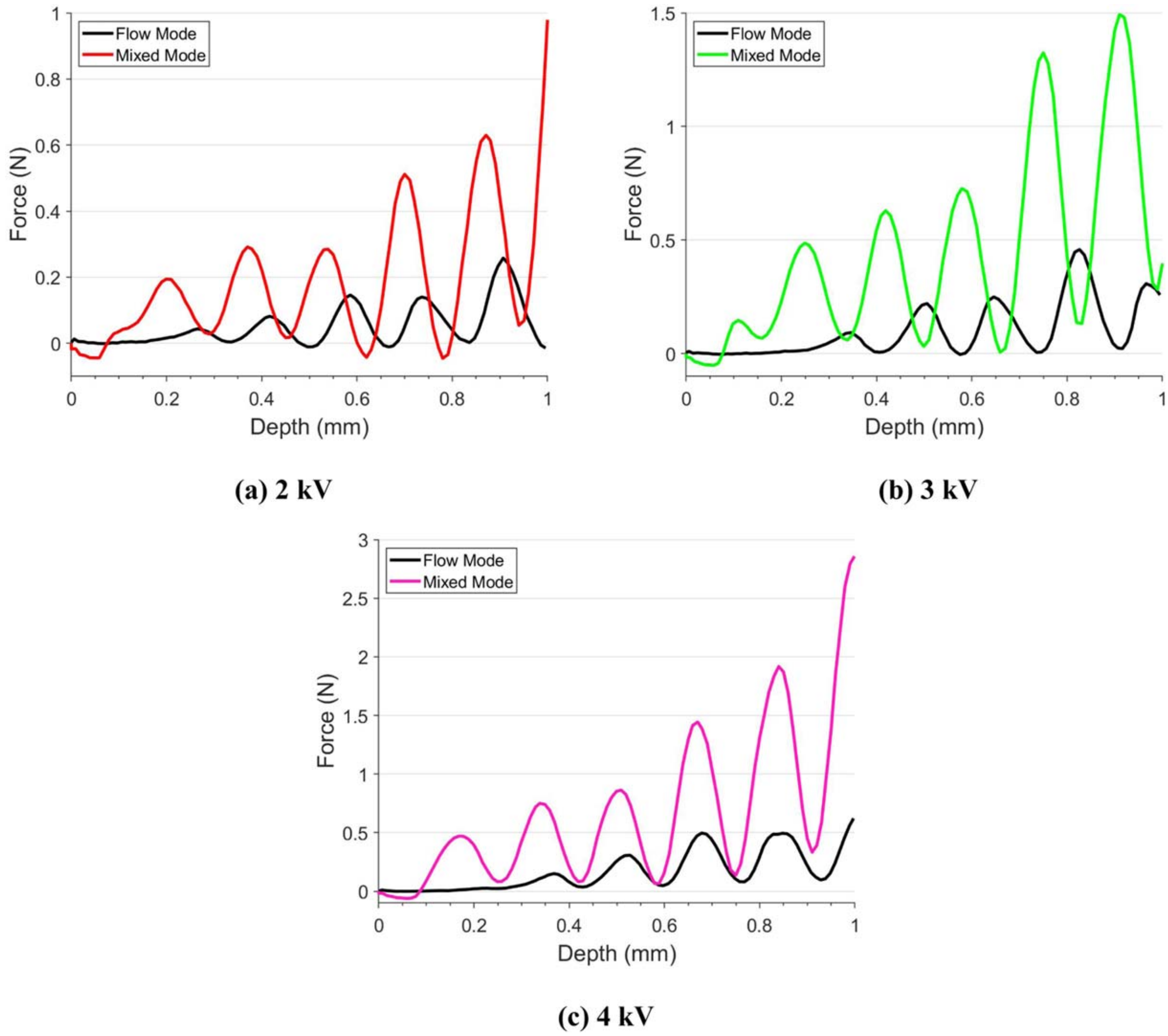

Figure 14. Comparison of vibrotactile feedback strictly due to the ER effect at 3 Hz excitation between the previous flow mode actuator [35] and the proposed mixed-mode actuator.

that of the previous, flow mode-based actuator [35]. To best compare the devices' fundamental principles (flow mode versus a mixed squeeze and flow mode), the force due to the fluid is isolated from the total force by removing the modeled forces associated with the membrane (for the flow mode design) and both the membrane and spring (for the mixed-mode design). Figure 14 compares the forces due to the ER fluid for the flow mode and mixed-mode actuator designs under a 3 Hz sine wave. As shown in the figure, the mixed-mode actuator produces greater amplitudes of vibration for a given voltage. Additionally, the mixed-mode actuator responds with vibration output earlier in the actuator's stroke than that of the flow mode design. Therefore, the introduction of squeeze mode within the mixed-mode design leads to a more dynamic haptic device.

4.4.2. High frequency. As previously discussed, humans are capable of sensing tactile signals at much higher frequencies than just the set tested in the previous subsection. For a complete evaluation of the device's tactile performance, this subsection examines performance at high frequencies up to 300 Hz, corresponding to the sensitivity of the Pacinian corpuscle. To measure the actuator's high frequency vibrotactile response, 4 kV square waveforms at frequencies of 50, 100, 200, and 300 Hz are supplied, and data is collected from the accelerometer at 2 kHz sampling rate. Data analysis is performed in both the time and frequency domains via fast Fourier transform (FFT).

Figure 15 presents the measured acceleration response for the tested frequencies (50, 100, 200, and 300 Hz). As shown in the time domain plots, prior to pressing, the magnitude of acceleration is close to 0 g. During the 1 mm press, the magnitude of acceleration increases. At 1 mm depth, the indenter reverses its direction and fluid flow pauses, indicated in the plot by a moment of 0 g acceleration. When the indenter reverses its direction, fluid flow resumes and the amplitude of vibration increases until the indenter stops at its initial position of 0 mm. As shown, the maximum vibration intensity generated by the actuator is 1.3 g. As the applied frequency increases, the maximum intensity decreases. At

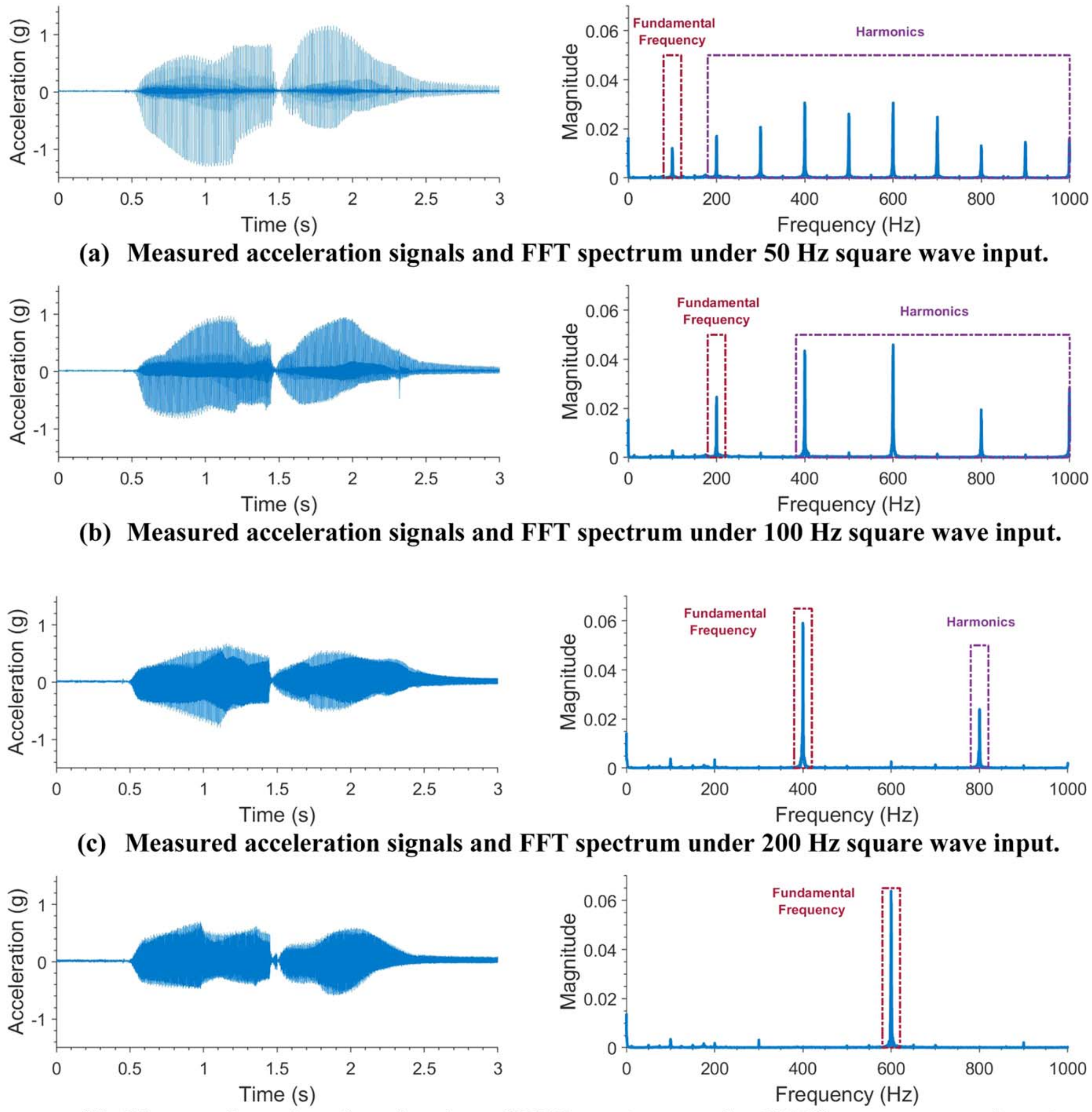

(a) Measured acceleration signals and FFT spectrum under 50 Hz square wave input.

(b) Measured acceleration signals and FFT spectrum under 100 Hz square wave input.

(c) Measured acceleration signals and FFT spectrum under 200 Hz square wave input.

(d) Measured acceleration signals and FFT spectrum under 300 Hz square wave input.

Figure 15. Measured acceleration signals and fast Fourier transformation (FFT) results for a wide range of input frequencies.

300 Hz, the maximum intensity is found to be 0.7 g. Psychophysical studies reveal that the human acceleration detection threshold is 0.01 g ($0.1\ \mathrm{m\,s^{-2}}$) for frequencies between 0 and 500 Hz [55]. As evidenced by the acceleration-time plots, the device can generate vibration intensities significantly greater than the 0.01 g threshold. Therefore, the actuator can convey distinct tactile sensations at high frequencies.

Figure 15 also presents the single-sided amplitude spectrum $|P1(f)|$ produced by FFT of the corresponding time domain data. It should be noted that the fundamental frequency found by the FFT analysis is twice that of the applied square wave frequency. As shown, for 50 Hz square wave input, the fundamental frequency is 100 Hz. This trend holds for the trials at other frequencies and may be attributed to the absolute nature of the resistive force posed by the fluid. Harmonics, integer multiples of the fundamental frequency, are seen in the FFT spectrums, as well. The FFT results validate that the actuator can accurately return vibrotactile feedbacks at the assigned frequency of the voltage input.

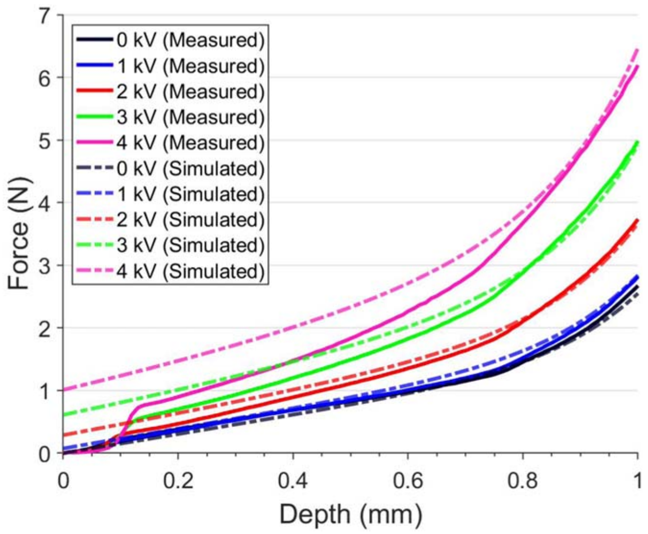

Figure 16. Comparison of kinesthetic feedback between the measured and simulated force for the mixed mode haptic actuator.

To summarize the high frequency analysis, the measured results demonstrate that the ERF haptic actuator can trigger the Pacinian corpuscle. The actuator is capable of conveying vibrotactile sensations to users in a wide frequency range, taking advantage of the full spectrum of human tactile perception.

4.5. Numerical versus experimental performance

The results predicted by the simulation (transparent, dashed lines) are compared to the results obtained experimentally (solid, opaque lines) in figure 16. As shown, the two methods agree to an acceptable extent. The model predicts non-zero starting force, which is not physically realizable in experiments; however, the experimental results do rise close to the modeled forces at about 0.1 mm. After 0.1 mm, the curves are closely aligned with little variance. In the case of 4 kV applied, the model slightly overestimates the force output.

Similarly, the modeled vibrotactile response may be compared to the experimental vibrotactile results. Figure 17 shows the measured and simulated results under application of a 3 Hz sine wave. As shown, the curves show reasonable correspondence for 1, 2, 3 and 4 kV.

Furthermore, the analytical model can be leveraged to gain insight into the actuator's experimental and simulated performance. Equation (1) presented a formulation for the force generated by the actuator, this study's primary performance metric. As shown analytically, the total force produced by the actuator can be attributed to the individual forces due to field-dependent yielding, viscous flow, and the elastic deformation of the spring and membrane. The forces due to yielding contribute the most to the actuator's ability to provide a wide range of forces, as the viscous and elastic components remain constant across all applied voltages. To create distinct forces (or maximization of the JND), the field-dependent forces associated with yielding should be maximized relative to the field-independent viscous and elastic forces, which provide the baseline force output. Additionally, the viscous forces can be shown to be dominated by the other forces present [56]; computing the sum of the squeeze and flow viscous forces from the analytical model and simulation input parameters results in 0.015 N at maximum depth, a relatively small contribution. The design choice of a spring electrode with a low spring constant and a soft elastomer membrane provide a low force output in the off-state, thus enabling high force rates when voltage is applied.

5. Conclusion

This study has presented the design, modeling and testing of a compact ER actuator for haptic feedback. The actuator built upon previous studies with modifications to incorporate a region of squeeze mode operation with a goal of (1) producing a wide range of forces and (2) vibrotactile feedback at frequencies up to 300 Hz. Implementing a squeeze mode via a thin, spring electrode came at little cost to the device's mechanical complexity and form factor. Experimental testing was performed using DMA fitted with an accelerometer and data acquisition system for high frequency analysis. The resistive force produced by the device along its stroke was measured for both kinesthetic (DC) and vibrotactile (AC sine waveform) input voltage signals. The results demonstrated that the mixed-mode actuator can provide up to 6.2 N of kinesthetic force at rates greater than the JND. Furthermore, the actuator can generate distinguishable vibrotactile feedback up to the perceivable limit of 300 Hz. Additionally, a mathematical model for the actuator's force output was described and developed into a computational model. Agreement between the experimental and computational results validated the model as a useful design tool.

The mixed-mode device can generate a wider range of sensations at finer resolution than the previous pure flow mode design. In fact, squeeze mode was found to be the dominant mode of producing force. Future design may center around squeeze mode because it can produce consistent forces even at low displacement. Removal of flow mode regions may also reduce the device's circumference, leading to better miniaturization. Furthermore, adopting an inclined plunger-based squeeze mode may allow for thickness reduction while maximizing force output.

The outcomes of this study demonstrate that the ER fluid-based device can provide wide-ranging haptic feedback to users. By delivering concurrent kinesthetic and tactile sensations across a wide spectrum, our sense of immersion when interacting with technology may be improved. The device may be used as a button in interactive systems such as telerobotics, gaming or automotive controls. To demonstrate more robust feedbacks, the actuator may be used as a haptic interface by embedding a pressure sensor and feedback

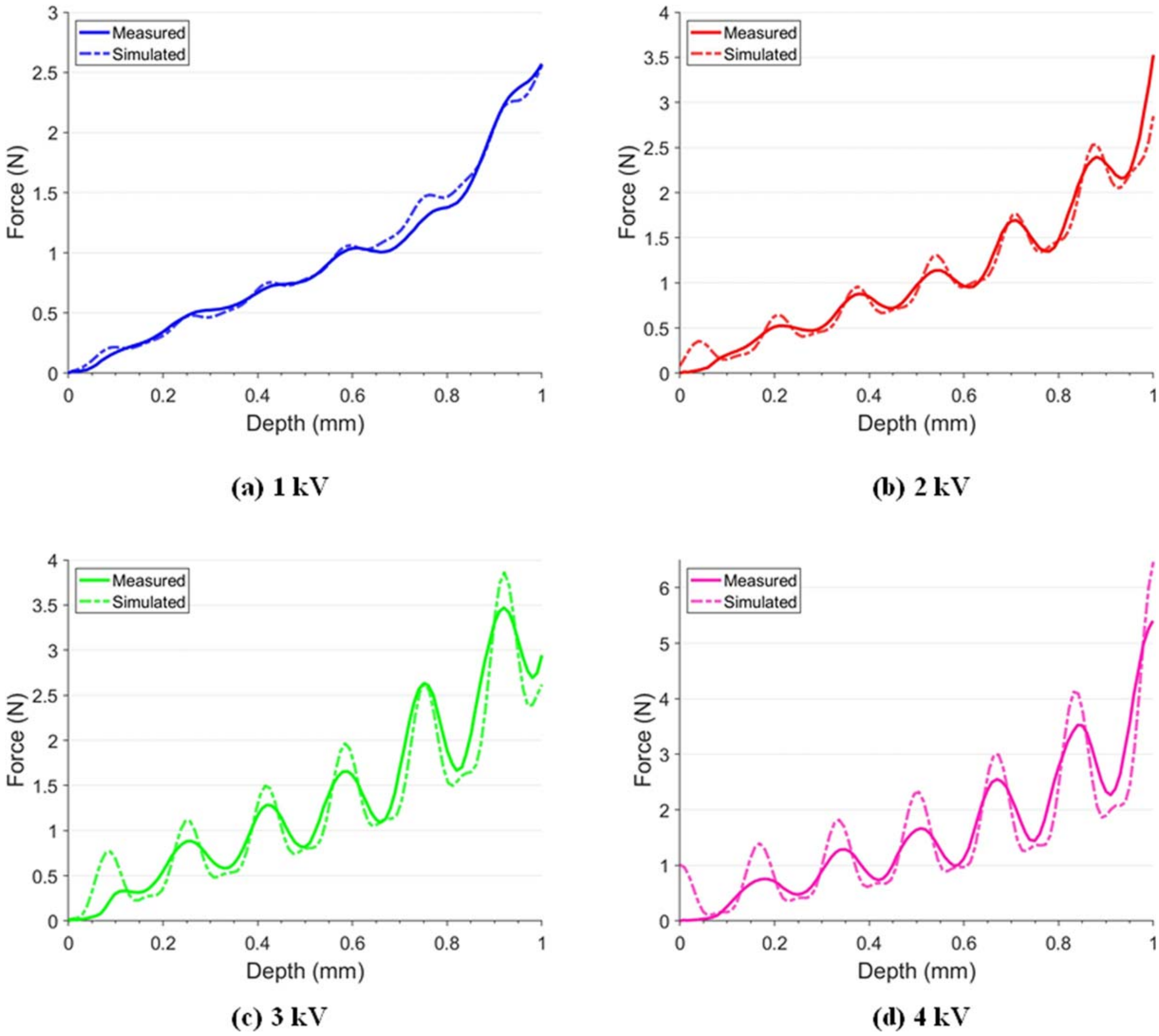

Figure 17. Comparison of vibrotactile feedback between the measured and simulated force for the mixed mode haptic actuator.

control to render realistic sensations between a user and virtual environment.

Acknowledgments

This work was supported by the National Research Foundation of Korea (NRF) grant funded by the Korea Government (MSIT) (No. 2018R1C1B5043837).

ORCID iDs

Jeong-Hoi Koo https://orcid.org/0000-0001-7740-8678
Tae-Heon Yang https://orcid.org/0000-0003-4316-4323

References

[1] Srinivasan M A and Basdogan C 1997 Haptics in virtual environments: taxonomy, research status, and challenges *Comput. Graph.* **21** 393–404

[2] Coles T R, Meglan D and John N W 2011 The role of haptics in medical training simulators: a survey of the state of the art *IEEE Trans. Haptic* **4** 51–66

[3] Laycock S D and Day A M 2003 Recent developments and applications of haptic devices *Comput. Graph. Forum* **22** 117–32

[4] Hayward V, Astley O R, Cruz-Hernandez M, Grant D and Robles-De-La-Torre G 2004 Haptic interfaces and devices *Sensor Rev.* **24** 16–29

[5] Eid M A and Al Osman H 2016 Affective haptics: current research and future directions *IEEE Access* **4** 26–40

[6] Lederman S and Klaztky R 2009 Haptic perception: a tutorial *Attention Perception Psychophys.* **71** 1439–59

[7] Lopes P and Baudisch P 2013 Muscle-propelled force feedback *Proc. SIGCHI Conf. on Human Factors in Computing Systems—CHI'13* pp 1–4

[8] Yang T-H, Kim S-Y, Kim C H, Kwon D-S and Book W J 2009 Development of a miniature pin-array tactile module using elastic and electromagnetic force for mobile devices *World Haptics 2009—3rd Joint EuroHaptics Conf. and Symp. on Haptic Interfaces for Virtual Environment and Teleoperator Systems (Salt Lake City, UT)* (Piscataway, NJ: IEEE) pp 13–7

[9] Schneider O, Shigeyama J, Kovacs R, Roumen J, Marwecki S, Boeckhoff N, Gloeckner D A, Bounama J and Baudisch P 2018 Dual panto: a haptic device that enables blind users to

continuously interact with virtual worlds *31st Annual ACM Symp. on User Interface Software and Technology—UIST'18* pp 877–87

[10] Gupta S and Campbell T 2010 Squeezeblock: using virtual springs in mobile devices for eyes-free interaction *Proc. 23nd Annual ACM Symp. on User Interface Software and Technology* pp 101–4

[11] Teng S, Wang C, Seyed T and Chen B 2019 Aarnio: passive kinesthetic force output for foreground interactions on an interactive chair *Proc. 2019 CHI Conf. on Human Factors in Computing Systems* pp 1–13

[12] An J and Kwon D-S 2002 Haptic experimentation on a hybrid active/passive force feedback device *Proc. 2002 IEEE Int. Conf. on Robotics and Automation* pp 4217–22

[13] Adams R J, Moreyra M R and Hannaford B 1998 Stability and performance of haptic displays: theory and experiments *Int. Mechanical Engineering Congress and Exhibition* (Anaheim: ASME) pp 227–34

[14] Biswas S and Visell Y 2019 Emerging material technologies for haptics *Adv. Mater. Technol.* **4** 1900042

[15] Qamar I P S, Groh R, Holman D and Roudaut A 2018 HCI meets material science: a literature review of morphing materials for the design of shape-changing interfaces *Proc. 18 CHI Conf. on Human Factors in Computing Systems—CHI'18* pp 1–23

[16] Poupyrev I and Maruyama S 2003 Tactile interfaces for small touch screens *Proc. 16th Annual ACM Symp. on User Interface Software and Technology* pp 217–20

[17] Rekimoto J and Schwesig C 2006 PreSenseII: bi-directional touch and pressure sensing interactions with tactile feedback *CHI'06 Extended Abstracts on Human Factors in Computing Systems—CHI EA'06* (New York: ACM) pp 1253–8

[18] Nakagawa Y, Kamimura A and Kawaguchi Y 2012 MimicTile: a variable stiffness deformable user interface for mobile devices *Proc. 2012 ACM Annual Conf. on Human Factors in Computing Systems—CHI'12* pp 745–8

[19] Hwang D, Lee J and Kim K 2017 On the design of a miniature haptic ring for cutaneous force feedback using shape memory alloy actuators *Smart Mater. Struct.* **26** 105002

[20] Chen D, Song A, Tian L, Zeng H and Xiong P 2019 Development of a multidirectional controlled small-scale spherical MR actuator for haptic applications *IEEE/ASME Trans. Mechatron.* **24** 1597–1607

[21] Jansen Y, Karrer T and Borchers J 2010 MudPad: localized tactile feedback on touch surfaces *Proc. 23nd Annual ACM Symp. on User Interface Software and Technology* pp 385–6

[22] Han Y M, Oh J S, Kim J K and Choi S B 2014 Design and experimental evaluation of a tactile display featuring magnetorheological fluids *Smart Mater. Struct.* **23** 077001

[23] Coon A, Yang T-H, Kim Y-M, Kang H and Koo J-H 2019 Application of magneto-rheological fluids for investigating the effect of skin properties on arterial tonometry measurements *Front. Mater.* **6** 45

[24] Yang T-H, Kwon H-J, Lee S S, An J, Koo J-H, Kim S-Y and Kwon D-S 2010 Development of a miniature tunable stiffness display using MR fluids for haptic application *Sensors Actuators* A **163** 180–90

[25] Yang T H and Koo J H 2017 Experimental evaluation of a miniature MR device for a wide range of human perceivable haptic sensations *Smart Mater. Struct.* **26** 125006

[26] Yang T H, Koo J H, Kim S Y and Kwon D S 2017 Modeling and test of a kinaesthetic actuator based on Mr fluid for haptic applications *Rev. Sci. Instrum.* **88** 035004

[27] Whittle M, Atkin R J and Bullough W A 1996 Dynamics of an electrorheological valve *Int. J. Mod. Phys.* B **10** 2933–50

[28] Choi S B, Cheong C C, Jung J M and Choi Y T 1997 Position control of an ER valve-cylinder system via neural network controller *Mechatronics* **7** 37–52

[29] Stangroom J 1983 Electrorheological fluids *Phys. Technol.* **14** 290–6

[30] Tsujita T, Kobayashi M and Nakano M 2010 Design and development of a braille display using micro actuators driven by ER suspension *Int. J. Appl. Electromagn. Mech.* **33** 1661–9

[31] Goto M and Takemura K 2013 Tactile bump display using electro-rheological fluid *IEEE Int. Conf. on Intelligent Robots and Systems* pp 4478–83

[32] Pfeiffer C, Mavroidis C, Bar-Cohen Y and Dolgin B 1999 Electrorheological fluid based force feedback device *Proc. 1999 SPIE Telemanipulator and Telepresence Technologies VI* pp 88–99

[33] Monkman G J 1992 An Electrorheological tactile display *Presence: Teleoperators Virtual Environ.* **1** 219–28

[34] Mazursky A, Koo J-H and Yang T-H 2018 Experimental evaluation of a miniature haptic actuator based on electrorheological fluids *Proc. SPIE* **10595** 105951M

[35] Mazursky A, Koo J-H and Yang T-H 2019 Design, modeling, and evaluation of a slim haptic actuator based on electrorheological fluid *J. Intell. Mater. Syst. Struct.* **30** 2521–33

[36] Chouvardas V G, Miliou A N and Hatalis M K 2008 Tactile displays: overview and recent advances *Displays* **29** 185–94

[37] Park G, Choi S, Hwang K, Kim S, Sa J and Joung M 2011 Tactile effect design and evaluation for virtual buttons on a mobile device touchscreen *Proc. 13th Int. Conf. on Human Computer Interaction with Mobile Devices and Services—MobileHCI '11 (Stockholm, Sweden)* p 11–20

[38] Hwang I and Choi S 2010 Perceptual space and adjective rating of sinusoidal vibrations perceived via mobile device *2010 IEEE Haptics Symp., HAPTICS 2010* pp 1–8

[39] Choi S-B and Hong S-R 2004 Dynamic modeling and vibration control of electrorheological mounts *J. Vib. Acoust.* **126** 537

[40] Goldasz J and Sapinski B 2012 Nondimensional characterization of flow-mode magnetorheological/electrorheological fluid dampers *J. Intell. Mater. Syst. Struct.* **23** 1545–62

[41] Phillips R 1969 Engineering applications of fluids with a variable yield stress *PhD Thesis* University of California Berkeley

[42] Williams E W, Rigby S G, Sproston J L and Stanway R 1993 Electrorheological fluids applied to an automotive engine mount *J. Non-Newtonian Fluid Mech.* **47** 221–38

[43] Dimock G A, Yoo J-H and Wereley N M 2002 Quasi-steady bingham biplastic analysis of electrorheological and magnetorheological dampers *J. Intell. Mater. Syst. Struct.* **13** 549–59

[44] Hong S-R, John S, Wereley N M, Choi Y-T and Choi S-B 2008 A unifying perspective on the quasi-steady analysis of magnetorheological dampers *J. Intell. Mater. Syst. Struct.* **19** 959–76

[45] Wang X and Gordanienejad F 1999 Flow Analysis of field-controllable, electro- and magneto-rheological fluids using herschel-bulkley model *J. Intell. Mater. Syst. Struct.* **10** 601–8

[46] Kamath G M, Hurt M K and Wereley N M 1996 Analysis and testing of bingham plastic behavior in semi-active electrorheological fluid dampers *Smart Mater. Struct.* **5** 576–90

[47] Hong S R, Choi S B, Jung W J and Jeong W B 2002 Vibration isolation of structural systems using squeeze mode ER mounts *J. Intell. Mater. Syst. Struct.* **13** 421–4

[48] Jolly M and Carlson J 1996 Controllable squeeze film damping using magnetorheological fluid *Proc. 5th Int.Conf. on New Actuators ((Bremen))* pp 333–6

[49] Wereley N M and Pang L 1998 Nondimensional analysis of semi-active electrorheological and magnetorheological dampers using approximate parallel plate models *Smart Mater. Struct.* **7** 732–43

[50] Vlassak J J and Nix W D 1992 A new bulge test technique for the determination of Young's modulus and Poisson's ratio of thin films *J. Mater. Res.* **7** 3242–9

[51] Vemuri S H, Jhon M S, Zhang K and Choi H J 2012 New analysis of yield stress on giant electrorheological fluids *Colloid Polym. Sci.* **290** 189–92

[52] Johnson K 2001 The roles and functions of cutaneous mechanoreceptors *Curr. Opin. Neurobiol.* **11** 455–61

[53] Tan H Z, Durlach N I, Beauregard G L and Srinivasan M A 1995 Manual discrimination of compliance using active pinch grasp: the roles of force and work cues *Perception Psychophys.* **57** 495–510

[54] Pang X D, Tan H Z and Durlach N I 1991 Manual discrimination of force using active finger motion *Perception Psychophys.* **49** 531–40

[55] Ryu J, Jung J, Park G and Choi S 2010 Psychophysical model for vibrotactile rendering in mobile devices *Presence: Teleoperators Virtual Environ.* **19** 364–87

[56] Coulter J P, Weiss K D and Carlson J D 1993 Engineering applications of electrorheological materials *J. Intell. Mater. Syst. Struct.* **4** 248–59